

## Quantitative Phase Imaging with a Scanning Transmission X-Ray Microscope

M. D. de Jonge,<sup>1,\*</sup> B. Hornberger,<sup>2</sup> C. Holzner,<sup>2</sup> D. Legnini,<sup>1</sup> D. Paterson,<sup>1,\*</sup> I. McNulty,<sup>1</sup> C. Jacobsen,<sup>2</sup> and S. Vogt<sup>1</sup>

<sup>1</sup>Argonne National Laboratory, 9700 South Cass Avenue, Argonne, Illinois 60439, USA

<sup>2</sup>Department of Physics and Astronomy, Stony Brook University, New York 11794, USA

(Received 11 July 2007; revised manuscript received 13 February 2008; published 22 April 2008)

We obtain quantitative phase reconstructions from differential phase contrast images obtained with a scanning transmission x-ray microscope and 2.5 keV x rays. The theoretical basis of the technique is presented along with measurements and their interpretation.

DOI: [10.1103/PhysRevLett.100.163902](https://doi.org/10.1103/PhysRevLett.100.163902)

PACS numbers: 42.30.Rx, 07.79.-v, 07.85.Tt

X-ray imaging techniques have long capitalized on absorption contrast, governed by the imaginary component  $\beta$  of the refractive index. More recently phase contrast techniques have exploited the higher contrast offered by the real component  $\delta$  of the refractive index at x-ray energies [1–13]. Full-field methods have considerable success in quantitative phase reconstruction [6–12]. However, these methods often cannot reconstruct specimens with significant absorption [6,12], usually greater than about 10%. Interferometric methods [4] may further be limited by phase-wrapping effects to determine the phase only modulo  $2\pi$  radians. Both the capabilities and the measurement geometry determine the application of these techniques; for example, quantitative full-field methods have been employed for tomography [10–13].

In this Letter we describe a quantitative technique for phase imaging with a scanning transmission x-ray microscope (STXM). Compatibility with the STXM geometry will enable the technique to be combined with fluorescence microscopy to determine elemental concentrations from a single x-ray measurement. We advance the imaging theory for this system, and use this to determine the conditions for differential phase contrast imaging. The technique is robust in the presence of absorption, intensity fluctuations, and noise. The effects of a novel differential absorption contrast (DAC) term are described.

The transmitted intensity has been used in electron [14], x-ray [15–19], and optical [20] scanning transmission microscopes to obtain differential phase contrast (DPC) images. The electron technique was recently adapted for x-rays and extended to provide quantitative information [5]. These analyses use a weak-specimen approximation to invert the contrast transfer function, and require the phase shift  $\delta kt$  and absorption  $\beta kt$  to be less than 0.1, which places severe restrictions on their application. The technique outlined in this Letter allows quantitative reconstruction of specimens with arbitrary total phase shift and without phase-wrapping effects.

In a STXM one usually employs a single element detector to obtain a transmission image of a specimen. Figure 1 shows a typical optical arrangement used for a STXM equipped instead with an annular quadrant detector

(AQD). Other investigations have used CCDs [21], quadrant [14] and three-segment [22] designs, and dedicated configurations optimized for combined differential interference contrast and DPC imaging [5,19]. Our current detector is optimized for DPC imaging [23].

The amplitude in the focal plane (with coordinate  $\vec{x}_f$ ) is related to the amplitude at the zone plate  $P(\vec{x}_z)$  [24]:

$$p(\vec{x}_f) = \frac{-ik}{2\pi f} \exp\left[\frac{ik\vec{x}_f \cdot \vec{x}_f}{2f}\right] \int P(\vec{x}_z) \times \exp\left[\frac{-ik\vec{x}_f \cdot \vec{x}_z}{f}\right] dA_z, \quad (1)$$

where  $f$  is the focal length of the lens and  $k$  the wave number. We assume coherent and uniform illumination of the zone plate. The effect of incomplete coherence is a broadening of the focus with a commensurate loss of resolution. The effect on the recovered phase of the slightly nonuniform illumination typical of STXM is negligible.

We approximate the amplitude at the detector plane located a distance  $z$  downstream of the focal plane using

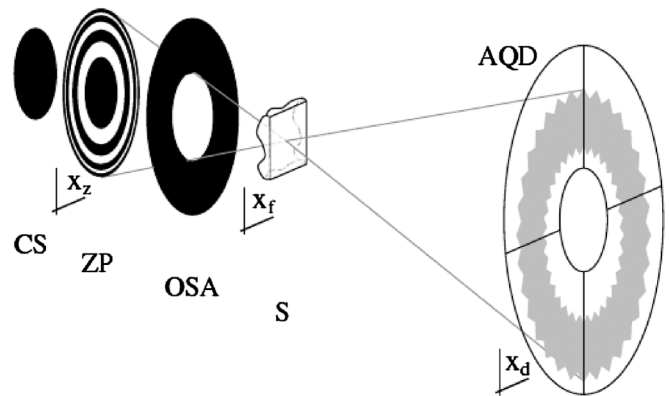


FIG. 1. Schematic of the optical elements used in a STXM equipped with an annular quadrant detector (AQD). The central stop (CS) and order-sorting aperture (OSA) block essentially all x-rays except those focused in the first diffraction order of the objective, a zone plate (ZP) lens. The specimen is scanned in the focal plane. The measured intensities can be used to determine the absorption and deflection of the beam imparted by the specimen.

Fraunhofer propagation, which is justified as  $z$  is typically several focal lengths [24]. Accordingly, the intensity in the detector plane with the specimen absent is

$$I_{d,0}(\vec{x}_d) = \left(\frac{k}{2\pi z}\right)^2 \left| \int p(\vec{x}_f) \exp\left[\frac{-ik\vec{x}_f \cdot \vec{x}_d}{z}\right] dA_f \right|^2. \quad (2)$$

We introduce a specimen into the focal plane by multiplying the focal-plane amplitude by the specimen function  $Q(\vec{x}_f) = \exp[in(\vec{x}_f)kt(\vec{x}_f)]$ , where  $t$  is the specimen thickness and  $n(\vec{x}_f) = -\delta(\vec{x}_f) + i\beta(\vec{x}_f)$  is the complex refractive index decrement. Expanding the phase and absorption terms in a Taylor series about the point illuminated by the beam (without loss of generality chosen to be 0) gives

$$Q(\vec{x}_f) \approx \exp[-i(\delta kt)_0 - (\beta kt)_0 - i\vec{x}_f \cdot \vec{\nabla}(\delta kt)_0 - k\vec{x}_f \cdot \vec{\nabla}(\beta kt)_0 + O(x_f^2)]. \quad (3)$$

Ignoring second-order terms for the present, the intensity in the detector plane is given by

$$I_d(\vec{x}_d) = \left(\frac{k}{2\pi z}\right)^2 \exp[-2(\beta kt)_0] \times \left| \int p(\vec{x}_f) \exp[-i\vec{x}_f \cdot \vec{\nabla}(\delta kt)_0 - \vec{x}_f \cdot \vec{\nabla}(\beta kt)_0] \times \exp\left[\frac{-ik\vec{x}_f \cdot \vec{x}_d}{z}\right] dA_f \right|^2. \quad (4)$$

The constant absorption term preceding the integral describes the absorption contrast used in most STXM measurements. The gradient terms within the integral are responsible for differential *phase* contrast (DPC) and differential *absorption* contrast (DAC), respectively. The DAC contribution is negligible when  $\frac{\delta}{\beta}$  is large and the probe  $p(\vec{x}_f)$  is small. In particular, the DAC term is negligible when it does not vary appreciably over the probe dimensions. As 95% of the intensity falls within the first 4 maxima of the focal spot [25], this condition requires

$$\exp\left[\frac{B_4 \delta_{R_N} |\vec{\nabla}(\beta kt)_0|}{\pi}\right] - \exp\left[\frac{-B_4 \delta_{R_N} |\vec{\nabla}(\beta kt)_0|}{\pi}\right] \ll 1, \quad (5)$$

where  $B_4 \approx 13.324$  is the fourth zero of the Bessel function and  $\delta_{R_N} = 50$  nm is the finest zone width of the zone plate. Presuming constant  $\beta$  and examining the limit in terms of a thickness variation, we require the thickness gradient  $\nabla(t)_0 \ll 144$  for carbon at 2.5 keV [26]. When DAC can be neglected, the intensity in the detector plane becomes

$$I_d(\vec{x}_d) = \left(\frac{k}{2\pi z}\right)^2 \exp[-2(\beta kt)_0] \times \left| \int p(\vec{x}_f) \exp\left[\frac{-ik\vec{x}_f}{z} \cdot \left(\vec{x}_d + \frac{z\vec{\nabla}(\delta kt)_0}{k}\right)\right] dA_f \right|^2 = \exp[-2(\beta kt)_0] I_{d,0}(\vec{x}'_d). \quad (6)$$

We have performed a change of variable in the detector plane given by  $\vec{x}'_d = \vec{x}_d + \frac{z\vec{\nabla}(\delta kt)_0}{k}$ , which follows from the Fourier shift theorem, and identified the resulting function of  $\vec{x}'_d$  as the no-specimen intensity determined in Eq. (2). The change of variable describes a shift of the intensity in the detector plane due to the specimen phase gradient. The angular deflection is  $\vec{\Delta} = -\vec{\nabla}(\delta t)_0$ , in agreement with the predictions of a simple refractive treatment [27]. It is interesting to note that deflection angles are typically of order 1  $\mu$ rad, the objective lens N.A. 5 mrad, and the specimen wedge angle 1 rad.

The second-order terms in the Taylor series expansion [Eq. (3)] are even, and so their Fourier transforms are even. These terms redistribute the amplitude symmetrically about the shifted center, with negligible effects on the center-of-mass of the intensity distribution. While third and higher odd orders can shift the center-of-mass of the intensity distribution, their effect is negligible due to the use of a focused probe, which restricts the contribution of these terms to the small values of  $\vec{x}_f$ . Our wave-propagation simulations show that the interaction of the specimen with the beam shifts the intensity in the detector plane as expected but also gives rise to intensity fringes. These fringes result from the higher order terms in Eq. (6), and, as discussed, do not affect the location of the center-of-mass of the intensity.

We use the quadrant detector to quantify the deflection of the intensity distribution, and define the signal  $\vec{S}$  with horizontal and vertical components  $S_x = (I_R - I_L)/I_{\text{TOT}}$  and  $S_y = (I_T - I_B)/I_{\text{TOT}}$  respectively, where  $I_T$ ,  $I_B$ ,  $I_R$ , and  $I_L$  refer to the counts recorded by the top, bottom, right, and left halves, and  $I_{\text{TOT}}$  is the sum of all counts. Normalizing the signal to the total intensity accounts for the average specimen absorption term in Eq. (6) and removes the effect of source intensity variations. Equation (6) describes the intensity in the detector plane as a shifted image of the objective pupil function magnified by the factor  $\frac{z}{f}$ . In the x-ray regime the shift is small and the intensity reaching the top half of the detector is

$$I_T \approx \left[\frac{1}{2} + \frac{2f\Delta_y}{\pi(R_{ZP} + R_{CS})}\right] I_{\text{TOT}}, \quad (7)$$

where  $\Delta_y$  is the vertical component of the beam deflection and  $R_{ZP}$  and  $R_{CS}$  are the radii of the zone plate and the central stop, respectively. Similar expressions can be derived for  $I_B$ ,  $I_R$ , and  $I_L$ . The DPC signal is given by

$$\vec{S} = \frac{-4f}{\pi k(R_{ZP} + R_{CS})} \vec{\nabla}(\delta kt)_0. \quad (8)$$

We have treated the  $S_x$  values to correct for detector misalignment and beam drift by requiring that each row of the image sums to zero, which is valid for an isolated specimen. A similar normalization was applied to  $S_y$ . Other treatments exist in cases where the specimen is not

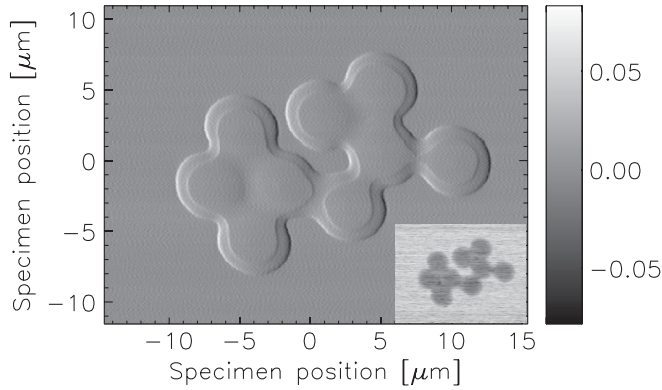


FIG. 2. Horizontal component of the DPC signal  $S_x$  obtained from a cluster of 5- $\mu\text{m}$ -diameter polystyrene spheres. The step within the spheres is due to the presence of residual solution. Inset: absorption contrast image obtained from the sum of all detector segments. The peak specimen absorption is about 7%. The scan was recorded in 401 by 301 steps of 75 nm using a 5-ms dwell.

isolated. Figure 2 shows  $S_x$  for a measurement of 5- $\mu\text{m}$ -diameter polystyrene spheres [28], taken at beam line 2-ID-B at the Advanced Photon Source. The x-ray probe was formed using a 160- $\mu\text{m}$ -diameter zone plate, a 40- $\mu\text{m}$ -diameter central stop, and a 30- $\mu\text{m}$ -diameter order-sorting aperture; the x-ray photon energy was 2.5 keV. The radius of the focal spot is approximately 60 nm [29] and the depth of focus approximately  $\pm 10 \mu\text{m}$  [30], and so the 5  $\mu\text{m}$  spheres are entirely within the focal plane. The specimen was prepared by placing a small drop of a 1:1 ethanol:water suspension of the spheres onto an electron microscopy grid. Most of the excess solution was wicked away with an absorbent cloth, leaving the spheres behind.

The reconstruction of gradient maps is a general physical problem. The Hartmann sensor has been used in observational astronomy and adaptive optics; reconstructions have used physical constraints to optimize orthonormal basis sets with least-squares fitting routines [31]. Various matrix approaches have been used [32,33], but these are computationally intensive. We use instead a Fourier integration technique [34,35]. The Fourier derivative theorem relates the two dimensional integral to the directional derivatives by

$$(\delta kt) = \mathcal{F}^{-1} \left[ \frac{\mathcal{F}[\nabla_x(\delta kt + i\nabla_y(\delta kt))]}{2\pi i(u + iv)} \right], \quad (9)$$

where  $\mathcal{F}$  denotes Fourier transformation, and  $u$  and  $v$  are reciprocal-space coordinates of the forward Fourier transform. The indeterminate zero-frequency term of Eq. (9) diverges due to the zero value of the denominator. In practice we prevent numerical instability by setting the zero-frequency element of the forward Fourier transform to zero, and the corresponding element of  $u + iv$  to a

nonzero value. We normalize the integrated phase so the average of the perimetric values is zero.

The integrated phase is given by the real part of Eq. (9). Nonzero elements in the imaginary part of Eq. (9) result from small “contradictions” in the derivatives, leaking power from the real to the imaginary component. As such, the imaginary component reflects errors in the reconstruction, and provides feedback for the accuracy of the integral. Here the imaginary part of Eq. (9) is less than about 10% of the real part, and the contradictions occur mostly at the perimeter of the spheres and at the ethanol:water meniscus, where DAC and higher order effects may be discernible. However, the influence of these few values on the integrated phase is mitigated by the use of a small step size.

Figure 3 presents the reconstructed thickness for the cluster of spheres. We interpreted the reconstructed phase as a thickness using the Henke tabulation [36] to determine  $\delta = 3.81 \times 10^{-5}$ , using  $\text{C}_8\text{H}_8$  for the molecular formula and a density of 1.05 g/cm<sup>3</sup> for polystyrene. The uncertainty associated with these assumptions is below about 10%. The data of Fig. 4 show the thickness profile along a line passing through one of the spheres. Also shown on this plot is the thickness profile that one would expect for a 5- $\mu\text{m}$  sphere added to a small sinusoidal background. The small deviations between the measured and calculated data (indicated) are due to the residual solution. The phase excursion of a single sphere is a little above 2.5 rad.

The two-dimensional integration is overconstrained, and determines a solution consistent with both directional derivatives. As a result there is a nonlocal relationship between the determined phase and the measured data, with the effect that the procedure is robust to noise. The detector signal-to-noise is of order 4000 [23], which corresponds here to a phase gradient of about  $1.5 \times 10^{-5}$  rad/nm or a carbon thickness gradient of about 1 part in 60. Because of

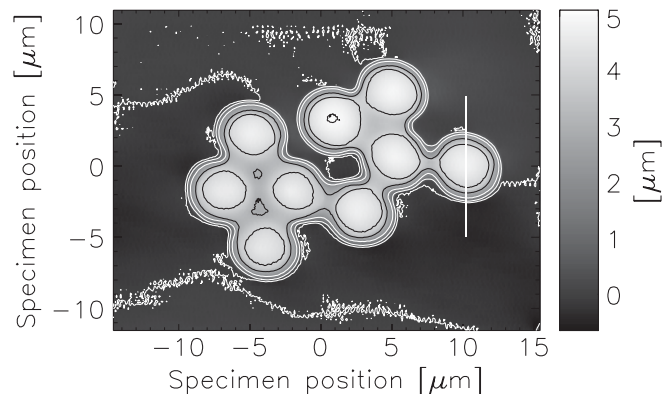


FIG. 3. Reconstructed thickness of the polystyrene spheres with contours shown at 1  $\mu\text{m}$  intervals. The unevenness of the contours is due to the residual solution. The thickness of the spheres can be determined despite the presence of this solution, and without detailed knowledge of its refractive index.

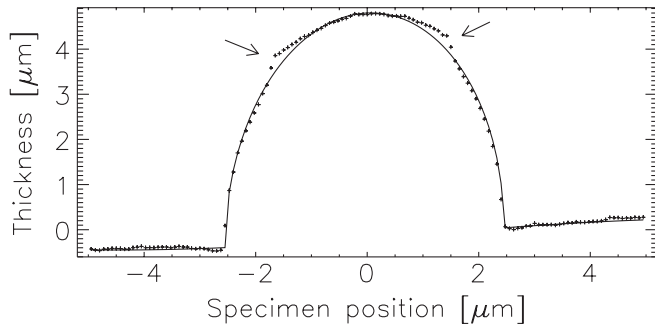


FIG. 4. Profile along the line through the rightmost sphere of Fig. 3. Points indicate the reconstructed thickness; the line indicates the thickness profile calculated for a 5- $\mu\text{m}$  sphere. A sinusoidal background was added to the calculated values to model the observed background variations. The measurements are in excellent agreement with the expected values. The residual fluid is clearly seen as a deviation from the spherical profile (arrows). At the center of the sphere the thickness of the fluid is zero, and so we can determine the thickness of the sphere without assuming the properties of the fluid.

the noise insensitivity of the integration we expect that this is a conservative estimate of the measurement sensitivity.

We have measured an object with dimensions and composition similar to a typical biological specimen. Assuming an average composition for, e.g., a cellular matrix will allow direct determination of cellular volumes and therefore also of trace elemental concentrations when used in conjunction with scanning fluorescence x-ray microscopy.

M. d. J. thanks B. F. Smith and T. S. Munson for discussions of numerical integration routines, C. Rau for help with the STXM, B. Tieman for computing assistance, and J. Arko for mechanical design and fabrication. Use of the Advanced Photon Source was supported by the U.S. Department of Energy, Basic Energy Sciences, Office of Energy Research, under Contract No. DE-AC02-06CH11357.

\*Present address: Australian Synchrotron, 800 Blackburn Road, Clayton 3168, Australia.

†martin.dejonge@synchrotron.org.au

- [1] A. Snigirev *et al.*, Rev. Sci. Instrum. **66**, 5486 (1995).
- [2] S. W. Wilkins *et al.*, Nature (London) **384**, 335 (1996).
- [3] P. Cloetens *et al.*, J. Phys. D **29**, 133 (1996).
- [4] U. Bonse and M. Hart, Appl. Phys. Lett. **6**, 155 (1965).
- [5] B. Hornberger, M. Feser, and C. Jacobsen, Ultramicroscopy **107**, 644 (2007).

- [6] K. A. Nugent, T. E. Gureyev, D. F. Cookson, D. Paganin, and Z. Barnea, Phys. Rev. Lett. **77**, 2961 (1996).
- [7] D. Paganin and K. A. Nugent, Phys. Rev. Lett. **80**, 2586 (1998).
- [8] B. E. Allman *et al.*, J. Opt. Soc. Am. A **17**, 1732 (2000).
- [9] F. Pfeiffer, T. Weitkamp, O. Bunk, and C. David, Nature Phys. **2**, 258 (2006).
- [10] A. Barty, K. A. Nugent, A. Roberts, and D. Paganin, Opt. Commun. **175**, 329 (2000).
- [11] P. J. McMahon *et al.*, Opt. Commun. **217**, 53 (2003).
- [12] P. Cloetens *et al.*, Appl. Phys. Lett. **75**, 2912 (1999).
- [13] F. Pfeiffer, C. Kottler, O. Bunk, and C. David, Phys. Rev. Lett. **98**, 108105 (2007).
- [14] N. H. Dekkers and H. de Lang, Optik (Jena) **41**, 452 (1974).
- [15] B. Kaulich *et al.*, Opt. Express **10**, 1111 (2002).
- [16] *X-ray Microscopy and Spectromicroscopy*, edited by J. Thieme, G. Schmahl, D. Rudolph, and E. Umbach (Springer, Berlin, 1998).
- [17] Y. Kagoshima *et al.*, Jpn. J. Appl. Phys. **43**, L1449 (2004).
- [18] A. Gianoncelli *et al.*, Appl. Phys. Lett. **89**, 251117 (2006).
- [19] M. Feser *et al.*, Nucl. Instrum. Methods Phys. Res., Sect. A **565**, 841 (2006).
- [20] W. B. Amos, S. Reichelt, D. M. Cattermole, and J. Laufer, J. Microsc. **210**, 166 (2003).
- [21] G. Morrison, W. J. Eaton, R. Barrett, and P. Charalambous, J. Phys. IV (France) **104**, 547 (2003).
- [22] B. C. McCallum, M. N. Landauer, and J. M. Rodenburg, Optik (Jena) **101**, 53 (1995).
- [23] B. Hornberger *et al.*, J. Synchrotron Radiat. (to be published).
- [24] J. W. Goodman, *Introduction to Fourier Optics* (McGraw-Hill, New York, 1968).
- [25] M. Born and E. Wolf, *Principles of Optics* (Cambridge University Press, Cambridge, England, 2002).
- [26] Evaluating the same expression for gold at 2.5 keV and 10 keV requires  $\nabla(t)_0 \ll 1$  and  $\nabla(t)_0 \ll 20$ , respectively, and so DAC contributions can be significant.
- [27] M. D. de Jonge *et al.*, Nucl. Instrum. Methods Phys. Res., Sect. A **582**, 218 (2007).
- [28] Fluka Micro particles based on polystyrene no. 79633, <http://www.sigmaaldrich.com/>.
- [29] H. M. Quiney *et al.*, Nature Phys. **2**, 101 (2006).
- [30] D. Attwood, *Soft X-Rays and Extreme Ultraviolet Radiation* (Cambridge University Press, Cambridge, England, 1999).
- [31] M. P. Rimmer, Appl. Opt. **13**, 623 (1974).
- [32] J. Herrmann, J. Opt. Soc. Am. **70**, 28 (1980).
- [33] W. H. Southwell, J. Opt. Soc. Am. **70**, 998 (1980).
- [34] M. R. Arnison *et al.*, J. Microsc. **214**, 7 (2004).
- [35] C. Kottler, C. David, F. Pfeiffer, and O. Bunk, Opt. Express **15**, 1175 (2007).
- [36] B. L. Henke, E. M. Gullikson, and J. C. Davis, At. Data Nucl. Data Tables **54**, 181 (1993).